

Technical Notes

Improved Prediction of Flow Around Airfoil Accreted with Horn or Ridge Ice

Maochao Xiao* and Yufei Zhang†
Tsinghua University, 100084 Beijing,
People's Republic of China
<https://doi.org/10.2514/1.J059744>

Nomenclature

C_p	=	pressure coefficient
c	=	airfoil chord length
f	=	frequency
Ma	=	Mach number
p	=	static pressure
Q	=	second invariant of velocity gradient tensor
Re	=	Reynolds number
U	=	time-averaged velocity
u, v, w	=	instantaneous velocity
x, y, z	=	Cartesian coordinates
$\langle \rangle$	=	mean flow quantity

Subscripts

rms	=	root mean square
∞	=	freestream quantity

I. Introduction

DESPITE advances in aircraft icing-protection systems, icing on aircraft lifting surfaces still poses a grave hazard to aircraft operation by decreasing the maximum lift and control-surface effectiveness, as well as increasing drag [1]. Ice shapes can be classified as roughness, streamwise ice, horn ice, and spanwise-ridge ice. Roughness is the most three-dimensional (3-D), and it usually causes low to moderate disturbances to flowfields. In contrast, the other three types are more two-dimensional (2-D) and have increased aerodynamic effects. In particular, the last two types are able to cause the most dramatic aerodynamic degradations.

Figure 1 illustrates the features of the circulation flow around an airfoil with leading-edge horn ice [1–3]. The flow separates at the tip of the horn because the boundary layer cannot withstand the adverse pressure required to keep the flow attached. Then, the Kelvin–Helmholtz (K-H) instability causes the separating shear layer (SSL) to roll up spanwise vortices. These vortices become 3-D while moving

downstream, which enhances mixing of the outer flow and the inner fluid, as well as reattaches the flow. Gurbachi [4] reported that the separated flow caused by spanwise-ridge ice has similar features as that induced by horn ice, except that the boundary layer has become mostly turbulent before reaching the ice accretion.

The accurate prediction of flow separation induced by horn/ spanwise-ridge ice places high demands on turbulence simulation methods. The limitations of the Reynolds-averaged Navier–Stokes (RANS) simulation method have been discussed in a recent review [5]. Use of the RANS method typically results in a remarkably long predicted separation bubble, which causes a severe underestimation of the lift [6]. Hybrid RANS/large-eddy simulation methods, such as the detached-eddy simulation (DES), are able to improve predictions of the integrated forces in iced-airfoil flows. For example, several authors [7–11] showed that the DES can predict lift curves that are in better agreement with experimental results for a GLC-305 airfoil with ice shape 944 (GLC-305/944) than RANS predictions. However, the flowfields are not improved commensurately. Two typical deviations between the predicted and experimental flowfields are given as follows:

1) The rollup of spanwise vortices is delayed in the initial SSL [7–11].

2) The predicted pressure recovery is much faster than observed. Figure 2 shows that the slopes of the surface pressure coefficients computed via DES-type methods [9,11] are steeper than in the experimental data.

The aim of this study is to improve the DES-type prediction of flow around airfoils with leading-edge horn ice (GLC-305/944 and NLF-0414/623) or spanwise-ridge ice (NACA-23012/EG1159). The improved delayed detached-eddy simulation (IDDES) method is combined with a vorticity-related subgrid length scale and a shear-layer-adapted subgrid length scale. The superiority of using both length scales over the original length scale is demonstrated.

II. Computational Methodology

A. Shear-Stress-Transport/Improved Delayed Detached-Eddy Simulation Method

The complete IDDES formulations with the $k-\omega$ shear-stress transport (SST) background RANS model can be found in Ref. [12]. The method consists of replacing the RANS length scale in the destruction term of the turbulent kinetic energy (TKE) equation with an IDDES hybrid length scale such that the model behaves as both RANS and LES in one simulation. The modified TKE equation is

$$\frac{\partial(\rho k)}{\partial t} + \frac{\partial(\rho u_j k)}{\partial x_j} = P_k - \frac{\rho k^{3/2}}{l_{IDDES}} + \frac{\partial}{\partial x_j} \left[(\mu + \sigma_k \mu_t) \frac{\partial k}{\partial x_j} \right] \quad (1)$$

where l_{IDDES} is the IDDES hybrid length scale defined as

$$l_{IDDES} = f_d(1 + f_e)l_{RANS} + (1 - f_d)l_{LES} \quad (2)$$

where $l_{RANS} = \sqrt{k}/C_\mu \omega$ and $l_{LES} = C_{DES}\Delta$ are the RANS turbulence length scale and the LES subgrid length scale, respectively. The term f_d is a blending function ranging between 0.0 (LES mode) and 1.0 (RANS mode). The subgrid scale Δ is given by

$$\Delta = \min\{\Delta_{wall}, \Delta_{free}\} \quad (3)$$

where Δ_{wall} and Δ_{free} are the subgrid length scales in the near vicinity of the walls and the regions free from wall effects, respectively.

Received 9 May 2020; revision received 21 January 2021; accepted for publication 22 January 2021; published online 4 March 2021. Copyright © 2021 by Maochao Xiao and Yufei Zhang. Published by the American Institute of Aeronautics and Astronautics, Inc., with permission. All requests for copying and permission to reprint should be submitted to CCC at www.copyright.com; employ the eISSN 1533-385X to initiate your request. See also AIAA Rights and Permissions www.aiaa.org/randp.

*Graduate Student, School of Aerospace Engineering; also Key Laboratory of Icing and Anti-/De-Icing, China Aerodynamics Research and Development Center, 621000 Mianyang, Sichuan, People's Republic of China. Student Member AIAA.

†Associate Professor, School of Aerospace Engineering; also Key Laboratory of Icing and Anti-/De-Icing, China Aerodynamics Research and Development Center, 621000 Mianyang, Sichuan, People's Republic of China; zhangyufei@tsinghua.edu.cn. Senior Member AIAA (Corresponding Author).

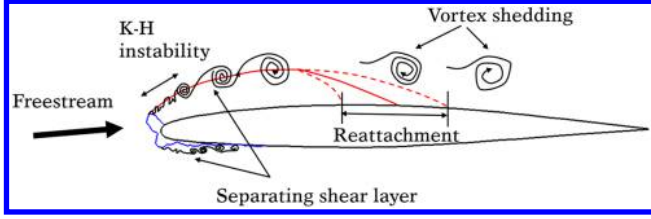


Fig. 1 Sketch of flow around an airfoil with leading-edge ice.

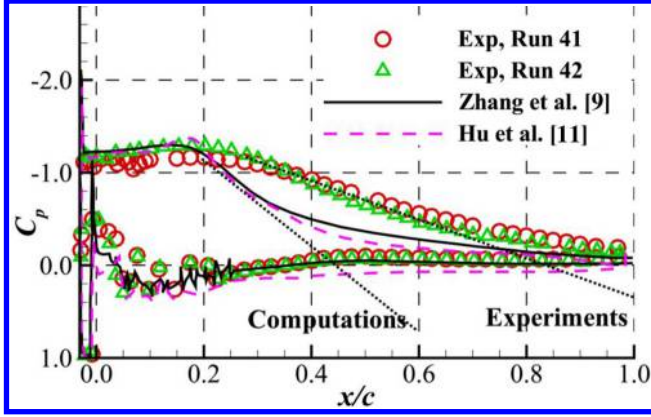


Fig. 2 Mean surface pressure coefficients predicted by DES-type methods for GLC-305/944 iced airfoil (dotted lines denote pressure recovery slopes). (Exp denotes experiment.)

B. Subgrid Length Scales

In the original version of SST-IDDES, Δ_{free} is taken as the maximum cell spacing:

$$\Delta_{\text{max}} = \max(\Delta_x, \Delta_y, \Delta_z) \quad (4)$$

However, when this length scale is used to compute a free shear layer, an excessively high eddy viscosity delays the K-H instability. This result is a so-called gray area issue. The high eddy viscosity can result from its excessive generation in the initial free shear layer and its convection from the RANS-modeled upstream turbulent boundary layer.

Mockett et al. [13], inspired by Chauvet et al. [14], proposed a vorticity-related subgrid length scale to address this issue:

$$\Delta_{\omega} = \frac{1}{\sqrt{3}} \max_{n,m=1,\dots,8} |\mathbf{n}_{\omega} \times \mathbf{r}_{mn}| \quad (5)$$

where \mathbf{n}_{ω} is the unit vorticity vector, and \mathbf{r}_{mn} is the vector formed by two arbitrary vertices of a cell. This length scale can be viewed as a projection of the edges and diagonals of a cell onto a vorticity plane, followed by applying the definition of Δ_{max} divided by $\sqrt{3}$ to the projected lengths. In the initial free shear layer in the x - y plane, the length scale is reduced to $\sqrt{(\Delta x^2 + \Delta y^2)}/3$, which is much smaller than $\Delta_{\text{max}} \sim \Delta z$ for pencil/book/ribbon cells [15]. Consequently, increased destruction of TKE [Eq. (1)] is obtained and reduction of the eddy viscosity is achieved in this region. More recently, Shur et al. [15] proposed a shear-layer-adapted subgrid length scale Δ_{SLA} that decreases Δ_{ω} further:

$$\Delta_{\text{SLA}} = \Delta_{\omega} F_{\text{KH}}(\langle \text{VTM} \rangle) \quad (6)$$

where $F_{\text{KH}}(\langle \text{VTM} \rangle)$ is an empirical function, and it is very small in the initial free shear layer where the flow is nearly 2-D. A complete description of Δ_{SLA} can be found in Ref. [15].

C. Other Numerical Methods

The present simulations were carried out using an in-house finite volume code [16,17]. The inviscid flux is discretized using a hybrid

central/upwind scheme [Eq. (7)], where a fourth-order central difference scheme is used to compute the central flux, and the Roe/fifth-order weighted essentially nonoscillatory scheme is used to calculate the upwind flux. The blending parameter is determined by Eq. (8) as in Ref. [18], where C_3 and C_4 are 4.0 and 0.6, respectively. Besides, σ_{min} is set as 0.1 in the present study. In separated regions, the ratio $l_{\text{IDDES}}/l_{\text{RANS}} < 0.6$ is met, which leads to $\sigma = 0.1$. The viscous flux is approximated using a second-order central difference scheme. Time integration is performed using the implicit dual-time-step lower-upper symmetric Gauss-Seidel scheme:

$$F_{\text{invisid}} = (1 - \sigma)F_{\text{central}} + \sigma F_{\text{upwind}} \quad (7)$$

$$\sigma = \max\left(\tanh\left(\frac{C_3}{1 - C_4} \max\left(\frac{l_{\text{IDDES}}}{l_{\text{RANS}}} - C_4, 0\right)\right), \sigma_{\text{min}}\right) \quad (8)$$

III. Numerical Results

A. Two Airfoils with Leading-Edge Horn Ice

Two airfoils (3-D extruded airfoils), the GLC-305/944 [19,20] and the NLF-0414 airfoil with ice 623 (NLF-0414/623) [21], are computed in this section. In aerodynamic experiments, both models have constant shapes in the spanwise direction. The freestream conditions are listed in Table 1. Figure 3 shows the computational grids in the x - y plane. The far-field boundaries are located approximately $50c$ away from the airfoils. Periodic boundaries are set in the spanwise direction, and adiabatic no-slip boundaries are applied at the walls. The grid details are provided in Table 2, where L_z is the spanwise size; N_{total} is the total cell number; N_x and N_z are the cell numbers in the circumferential and spanwise directions, respectively; $N_{x,\text{ice1}}$ and $N_{x,\text{ice2}}$ are the cell numbers along the upper and lower ice shapes, respectively; and Δy_w is the first-layer cell height. For GLC-305/944, a coarse grid is obtained by coarsening the fine grid approximately 1.2–1.3 times in each direction. Figure 4 shows the grid resolutions of the fine grid for GLC-305/944. On the upper surface, $\Delta x^+ < 220$ and $\Delta z^+ < 1$ are met for the first-layer cells. In the SSL, the number of grid points is 16, 24, and 28 in the vorticity thickness for $x/c = 0.15$, $x/c = 0.10$, and $x/c = 0.05$, respectively. In the simulations, the physical time step $\Delta t U_{\infty}/c$ is 0.001, and this time step is small enough to make sure $\Delta t U_{\infty}/\Delta x < 1.0$ is met for the most separation region aft of ice accretion. Within each physical time step, 40 subiterations are applied to achieve a second-order accuracy. For each case, about $20c/U_{\infty}$ is collected for statistics after the flow becomes fully developed.

Figure 5 compares the mean streamwise velocity fields obtained by different approaches with corresponding experimental measurements [19,20] for GLC-305/944. The flowfields are dominated by a separation bubble. Consequently, a blue region with $\langle u \rangle/U_{\infty} < -0.2$ can be observed in each field. Table 3 shows the streamwise lengths of the blue regions obtained using different methods. The grid refinement yields more accurate lengths for all three computational approaches (that is, using Δ_{max} , Δ_{ω} , and Δ_{SLA}), which indicates favorable grid convergence. Replacing Δ_{max} with either Δ_{ω} or Δ_{SLA} in either the fine or coarse grid yields larger lengths that are in better agreement with the experimental data.

The velocity profiles along lines L1–L3 (Fig. 5) are shown in Fig. 6 for the fine grid. Lines L1 and L2 occur before the bubble core. It can be observed that using both Δ_{ω} and Δ_{SLA} yields profiles that are consistent with the experimental data. By contrast, using Δ_{max} results in much steeper velocity gradients, indicating smaller growth rates before the bubble core. The corresponding predicted bubble core is consequently shifted further downstream. Line L3 is near the

Table 1 Freestream conditions

Cases	Ma	Re	AOA
GLC-305/944	0.12	3.5×10^6	6.0
NLF-0414/623	0.21	4.6×10^6	5.2

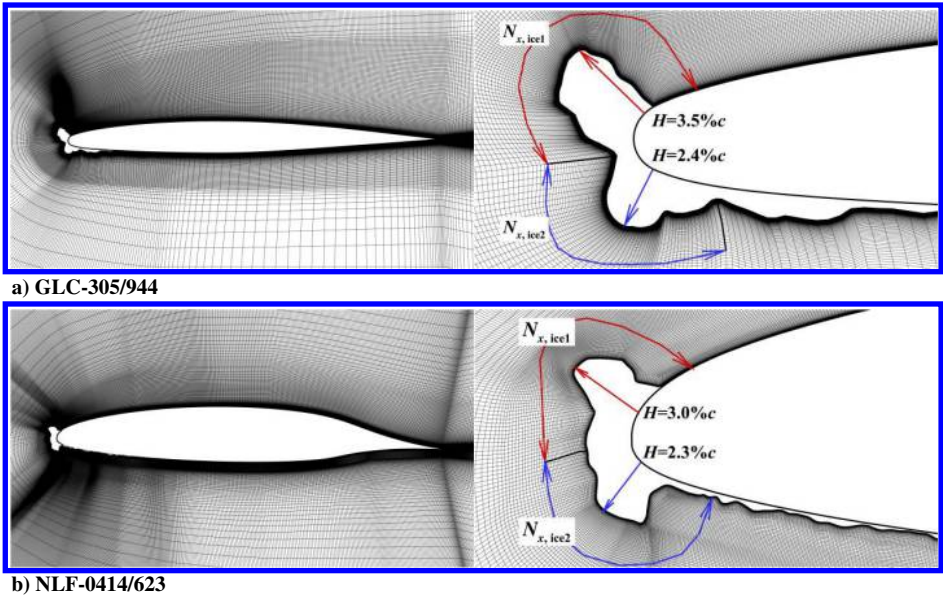


Fig. 3 Computational grids in x-y plane.

Table 2 Grid descriptions

Cases	N_x	N_z	$N_{x,ice1}$	$N_{x,ice2}$	N_{total} (millions)	L_z/c	$\Delta y_w/c$
GLC-305/944, fine	1148	160	156	40	30.04	0.4	7.0×10^{-6}
GLC-305/944, coarse	948	136	132	32	17.55	0.4	7.0×10^{-6}
NLF-0414/623	1164	160	120	108	27.35	0.2	6.0×10^{-6}

reattachment point. Using Δ_{max} clearly yields larger velocity values below $((y - y_{surf})/c = 0.04$, which is consistent with a much faster reattaching process aft of the bubble core as shown in Fig. 5. This result corresponds to overpredicted mixing aft of the bubble core. In contrast, using the two novel length scales produces profiles in agreement with the measured data.

The overpredicted mixing aft of the bubble core using Δ_{max} also influences the wall pressure coefficients. Figure 7a is a comparison of the wall pressure coefficients for the GLC-305/944 case. Two experimental datasets, “run 41” and “run 42,” are used as references [19,22]. They were both acquired via pressure taps, and the differences between them are due to experimental repeatability combined with digitization errors. The ice-induced separation bubble produces a clear plateau in the pressure distribution followed by pressure recovery on the suction side. The pressure plateaus predicted using the three methods are almost coincident. However, the curve

obtained using Δ_{max} exhibits a much faster pressure recovery. By contrast, using the other two length scales results in pressure recoveries that are in better agreement with the experimental results. Figure 7b is a comparison of pressure coefficients for NLF-0414/623. The experimental pressure plateau is a lot shorter than in the GLC-305/944 case. Using the two novel length scales offers the same advantages as for GLC-305/944.

Figure 8 shows the turbulent structures identified using the Q criterion for both iced airfoils. The flow separates off the ice tip; after which, the K-H instability grows by rolling up spanwise vortices. These structures gradually develop distortions and evolve into 3-D vortices, such as hairpin vortices, via a secondary instability. This evolution pattern is well resolved using Δ_ω and Δ_{SLA} . By contrast, the use of Δ_{max} delays the rollup of vortices. In addition, conspicuous large-scale spanwise structures are formed before flow reattachment. These large structures lead to the stronger mixing mentioned before

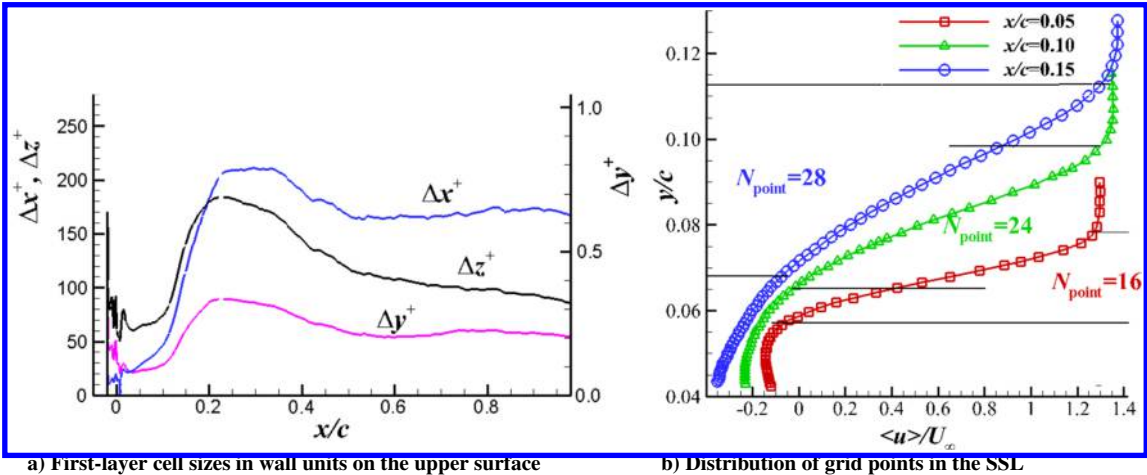


Fig. 4 Grid resolutions in different regions for the fine grid of GLC-305/944.

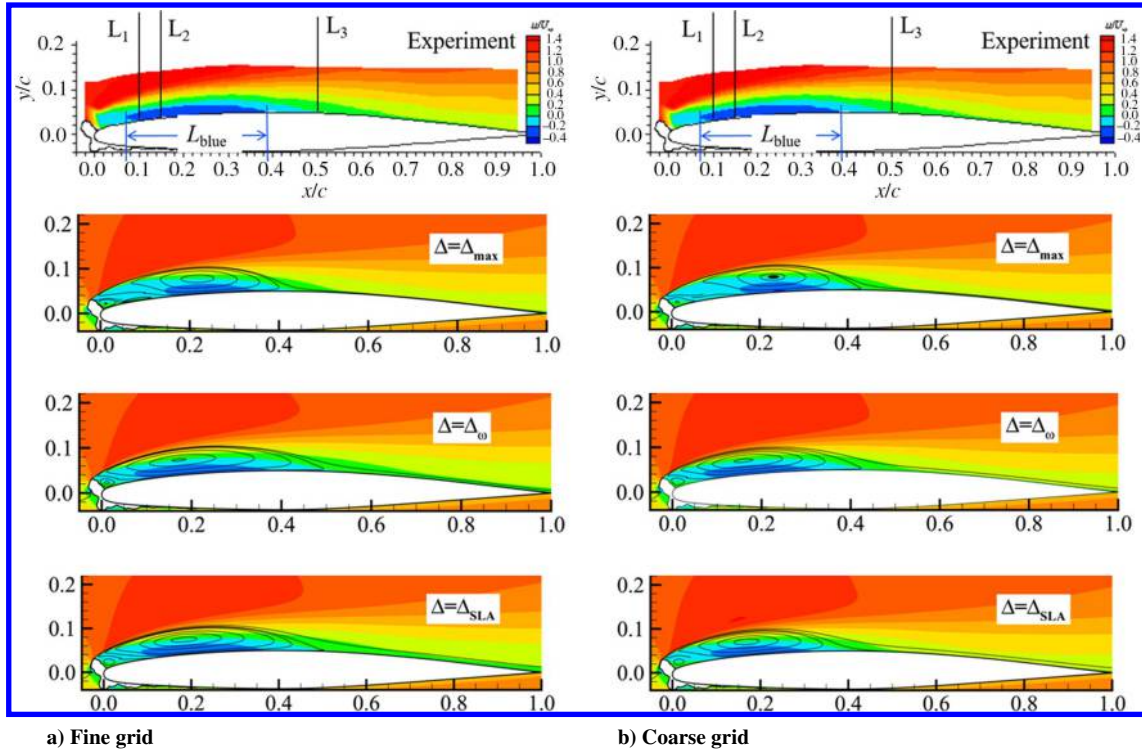


Fig. 5 Comparisons of mean streamwise velocity fields from experiment and computations (the experimental field picture is adapted from Ref. [20] and reprinted in part with permission from the AIAA).

Table 3 Streamwise length L_{blue} of blue regions ($\langle u \rangle / U_\infty < -0.2$; see Fig. 5) from experiment [19] and computations for two grids

Cases	$\Delta = \Delta_{max}$	$\Delta = \Delta_\omega$	$\Delta = \Delta_{SLA}$
Experiment [19]	0.32	0.32	0.32
Fine grid	0.20	0.30	0.29
Coarse grid	0.18	0.26	0.24

that results from using Δ_{max} . This will be clearly demonstrated later by a frequency analysis. The isosurfaces for NLF-0414/623 demonstrate similar advantages by using Δ_ω and Δ_{SLA} , although the separation bubble length is smaller than in the GLC-305/944 case. The improvement in these isosurfaces over those obtained using Δ_{max} can be explained using the contours of the eddy viscosity for GLC-305/944 shown in Fig. 9. Lower eddy viscosities are obtained using the two novel scales compared to using Δ_{max} . This result is especially true in the initial SSL because the smaller Δ_ω and Δ_{SLA} introduce larger destructions of TKE [Eq. (1)].

The preceding results show that ice accretions induce strong unsteadiness. Figure 10 displays the rms of the pressure coefficient

fluctuations obtained using $\Delta = \Delta_{SLA}$ and the fine grid for GIC-305/944. High-pressure fluctuations can be clearly observed along the SSL. In the following discussion, the fluctuations obtained using the different methods are compared in three zones: the shear-layer region, the reattachment region, and the attached flow region.

1. Fluctuations in Shear-Layer Region

Figures 11a and 11b show the power spectrum density (PSD) of the pressure fluctuations at points P1 and P2. The spectra obtained using Δ_{max} exhibit much lower PSD levels because of the delayed growth of turbulent fluctuations. In all three spectra, a high-frequency peak f_1 can be observed at P1. The peak frequency values are listed in Table 4. These peaks are associated with vortex motions from the K-H instability in the initial SSL. The nondimensional expression (i.e., Strouhal number) for the peak is [23]

$$St_\delta = \frac{f_1 \delta_\omega}{\bar{U}} \quad (9)$$

where the vorticity thickness of the SSL is $\delta_\omega = (U_{high} - U_{low}) / \max(\partial U / \partial n)$ (n denotes the shear normal direction), and the mean velocity is $\bar{U} = (U_{high} + U_{low}) / 2$. The values of the quantities

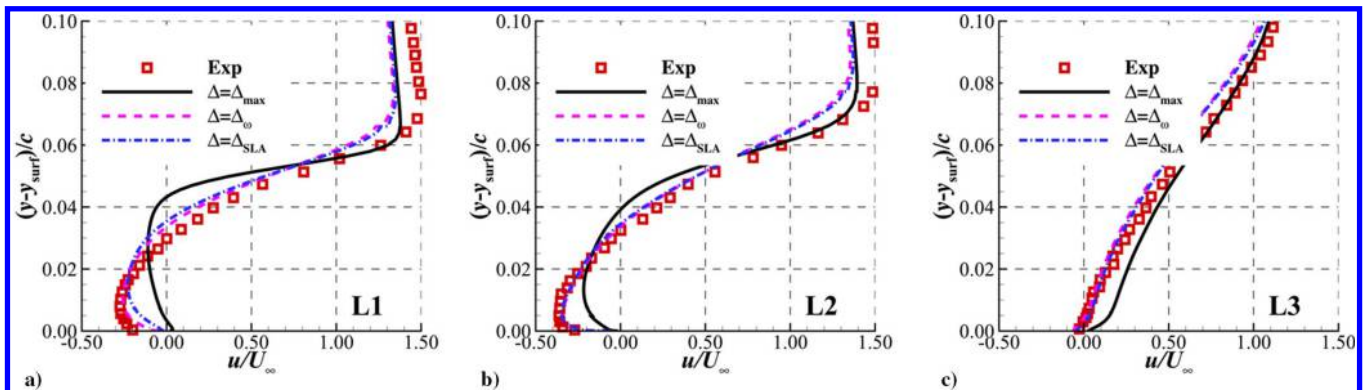


Fig. 6 Mean streamwise velocity profiles along L1-L3 from experiments [19] and computations for the fine grid.

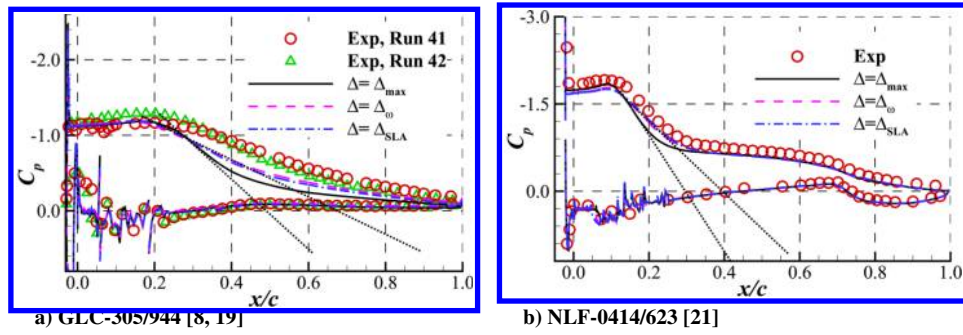


Fig. 7 Surface pressure coefficients from experiments [8,19,21] and computations for fine grids (dotted lines denote pressure recovery slopes).

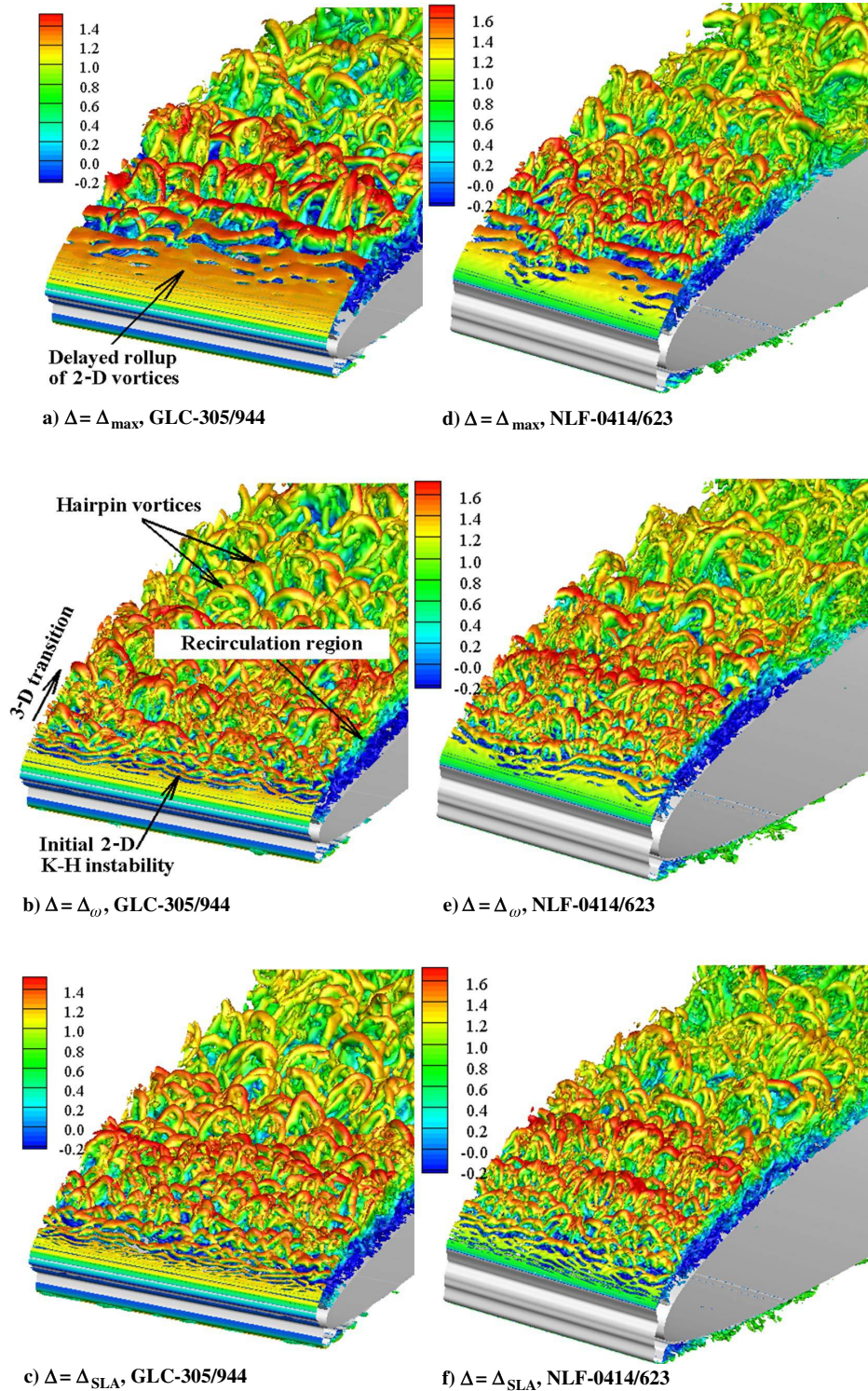


Fig. 8 Instantaneous isosurfaces of $Q(c/U_\infty)^2 = 200$ for GLC-305/944 and $Q(c/U_\infty)^2 = 500$ for NLF-0414/623 colored by streamwise velocity u/U_∞ .

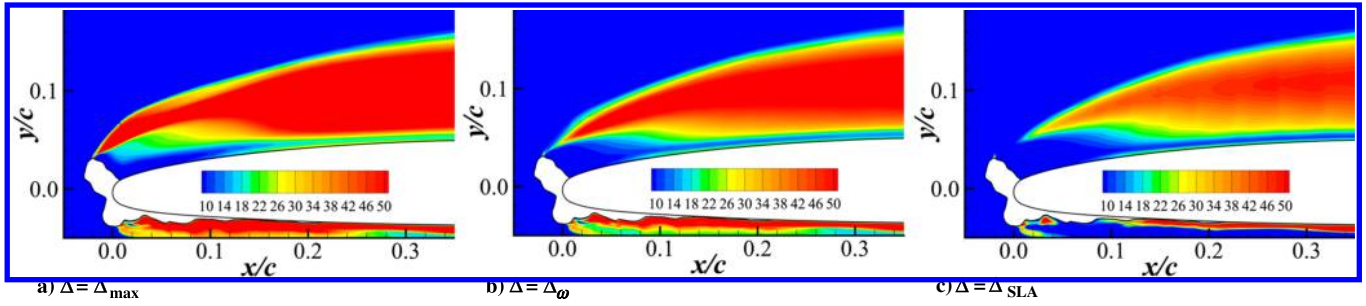


Fig. 9 Contours of mean μ_t/μ_∞ obtained from different approaches for GLC-305/944.

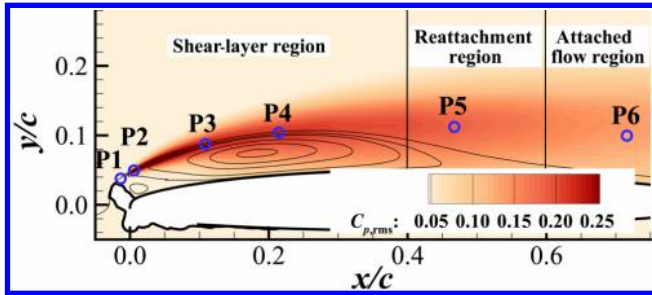


Fig. 10 RMS of pressure coefficient fluctuations using $\Delta = \Delta_{SLA}$ and fine grid for GLC-305/944.

required to compute St_δ are listed in Table 4. Using Δ_{max} , Δ_ω , and Δ_{SLA} results in calculated St_δ values of 0.124, 0.120, and 0.129, respectively. These values are in the same range as the typical value of 0.143 for a canonical mixing shear layer [23]. Note, however, that Δ_{max} significantly retards the rollup of 2-D vortices, as evidenced by the remarkably low PSD levels at P1 and P2.

In addition to a high-frequency f_1 , each spectrum exhibits a low-frequency f_2 . For $\Delta = \Delta_\omega$ and $\Delta = \Delta_{SLA}$, f_2 is exactly half the high frequency, indicating that the low frequency results from vortex pairing. Similar results for other flows have been reported by Deck and Larauie [24] and the Xiao et al. [16]. As a contrast, using Δ_{max}

does not capture this vortex pairing correctly because of the clear discrepancy between f_2 and $f_1/2$ (Table 4).

Figure 11c shows the spectra at P3. Using $\Delta = \Delta_{max}$ results in a conspicuous broadband peak at approximately $fc/U_\infty = 11$. This peak moves in the low-frequency direction and broadens from P3 to P4 (Fig. 11d). This peak is associated with the motions of spanwise structures, as shown in Fig. 12 by the cyan lines and the alternating low-pressure and high-pressure spots in the grayscale slice. Large-scale features cause high turbulent fluctuations, as evidenced by the streamwise velocity fluctuations at $x/c = 0.20$ (Fig. 13a). High fluctuations further lead to overly rapid reattachment, as shown in Figs. 5a and 7a. By contrast, the spectra obtained using $\Delta = \Delta_\omega$ and $\Delta = \Delta_{SLA}$ exhibit less conspicuous peaks and are in better agreement with the $-5/3$ law in the inertial range. But, it should be noted that spanwise coherent structures also appear as marked in Fig. 12.

2. Fluctuations in Reattachment Region

In Fig. 10, P5 is located in the reattachment region. The spectra at this location are displayed in Fig. 14a. There are clear peaks in the three spectra at approximately $fc/U_\infty = 1.46$. These peaks reflect the regular vortical shedding mode near the reattachment region. Mabey [25] showed that this frequency should be nondimensionalized by the separation bubble length. Consequently, the calculated Strouhal numbers St based on separation bubble length and free-stream velocity are 0.67, 0.78, and 0.76 for Δ_{max} , Δ_ω , and Δ_{SLA} ,

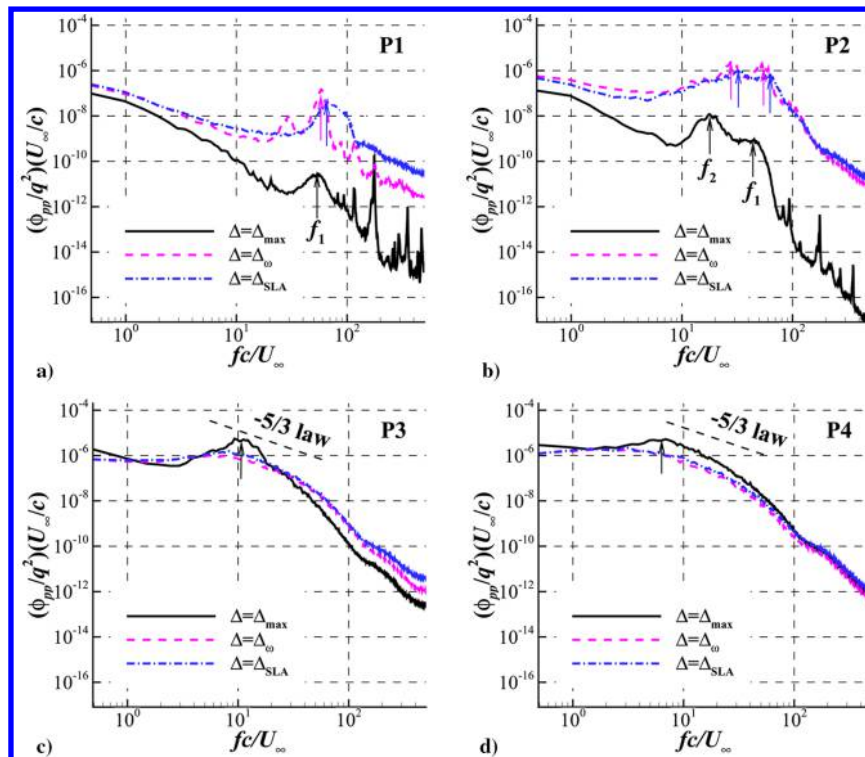
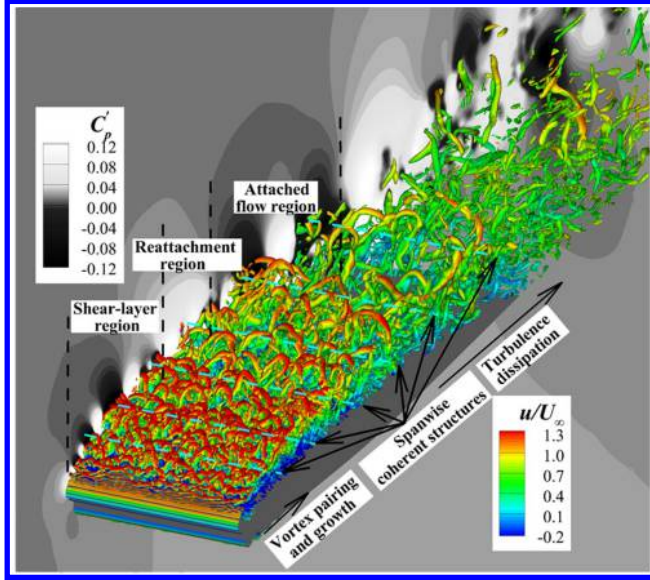


Fig. 11 PSD of pressure fluctuations at points P1–P4.

Table 4 Vortex-shedding frequencies resulting from K-H instability obtained using different methods

Length scales	$U_{\text{high}}/U_{\infty}$	$U_{\text{low}}/U_{\infty}$	δ_{ω}	$f_1 c/U_{\infty}$	St_{δ}	$f_2 c/U_{\infty}$	$f_1 c/2U_{\infty}$
$\Delta = \Delta_{\text{max}}$	1.43	3.56×10^{-2}	1.71×10^{-3}	52.00	0.124	18.04	26.00
$\Delta = \Delta_{\omega}$	1.40	2.71×10^{-2}	1.20×10^{-3}	58.55	0.120	30.24	29.28
$\Delta = \Delta_{\text{SLA}}$	1.41	3.76×10^{-2}	1.29×10^{-3}	64.53	0.129	31.82	32.27

**Fig. 12** Instantaneous Q isosurfaces for GLC-305/944 ($Q(c/U_{\infty})^2 = 500$) obtained using Δ_{SLA} and fine grid, where different colors show levels of streamwise velocity; grayscale slice shows pressure coefficient fluctuations.

respectively. These values lie in the range of 0.5–0.8 for various separated flows [25] and, to some extent, can also fit with the values of 0.60–0.65 for a NACA-0012 airfoil with the horn-ice shape studied by Ansell and Bragg [2,26]. Note that in Fig. 14a, a linear scale is used for the y axis instead of a log scale as for other locations. This is because the peaks associated with the regular vortical shedding will not look that conspicuous if a log scale is used for the y axis, which is also the reason that a linear scale is used in Refs. [2,26].

3. Fluctuations in Attached Region

Figure 13b compares the calculated streamwise velocity fluctuation profiles with experimental measurements at $x/c = 0.75$. Using Δ_{ω} or Δ_{SLA} produces fluctuation levels that are in agreement with the experimental data. By contrast, using Δ_{max} overly dissipates the fluctuations. The same conclusion can also be drawn from the

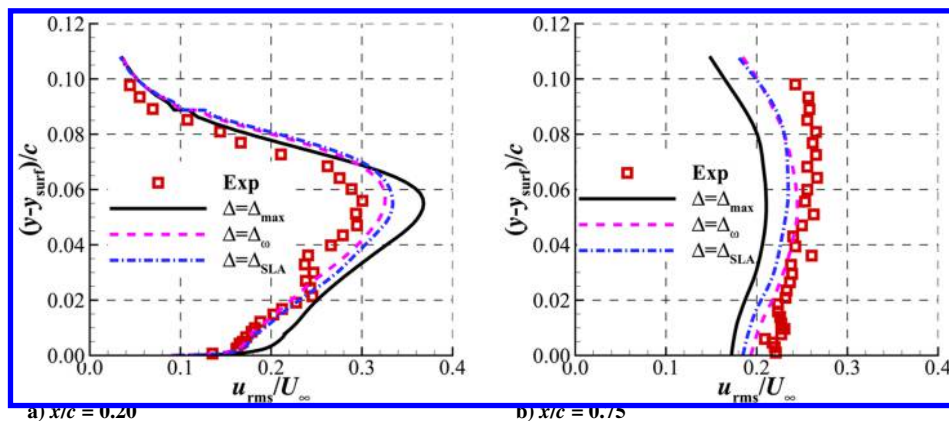
spectra at P6 (Fig. 14b), where using Δ_{max} results in lower PSD levels in the low-frequency part.

B. Airfoil with Spanwise-Ridge Ice

The NACA-23012 case with spanwise-ridge ice EG1159 (NACA-23012/EG1159) is investigated [27]. As shown in Fig. 15, the upper ice is accreted at $x/c = 6.0\%$ with a height $H/c = 1.4\%$, and the lower ice is accreted at $x/c = 11.0\%$ with a height $H/c = 0.6\%$. This iced airfoil is one of the most representative of ridge-ice configurations [27]. Although there are some spanwise variations in the ice accretion in the aerodynamic experiment, the ice is considered as 2-D here in the present study as in Refs. [28,29]. No spanwise variations are considered. The freestream conditions are $Ma = 0.20$, $Re = 15.74 \times 10^6$, and an angle of attack (AOA) of 2.0 deg. The major difference between the spanwise ice case and the aforementioned horn-ice cases is that it has a much longer attached boundary layer before separation. The grid details are listed in Table 5. A baseline grid (17.47 million cells), a coarse grid (9.16 million cells), and a fine grid (32.50 million cells) are used.

Figure 16 is a comparison of the calculated mean surface pressure coefficients with experimental data [27]. For the coarse grid, all three methods yield coincident distributions with the measured data for the upper surface, although using Δ_{ω} and Δ_{SLA} produces slightly better results. By contrast, they result in remarkable differences for the lower surface. The constant-pressure plateau is captured correctly by using Δ_{ω} or Δ_{SLA} , but it is significantly longer and at a higher pressure when Δ_{max} is used. Such a result is also obtained for the baseline grid (Fig. 16b). Regarding the mean lift coefficients, the calculated value is 0.268 from using Δ_{max} and the baseline grid, and it is a lot lower than the experimental value of 0.280 [27]. In contrast, the values obtained via Δ_{ω} and Δ_{SLA} are 0.276 and 0.278, which can fit better with the experiment. Figure 17 further compares the mean surface pressure coefficients obtained via the three sets of grids. The difference between the results from the baseline grid and from the fine grid is pretty small, which indicates that grid convergence has been achieved here.

The extended pressure plateaus obtained using Δ_{max} reflect the longer distance from the ice tip to the separation bubble core. Using Δ_{max} delays the generation of resolved TKE, which in turn considerably delays the start of reattachment compared to using Δ_{ω} or Δ_{SLA} (see Fig. 16). Figure 19 is a comparison of the instantaneous Q isosurfaces. The spanwise rollers aft of the ice shape are captured

**Fig. 13** RMS of streamwise velocity fluctuations from experiments [19] and computations.

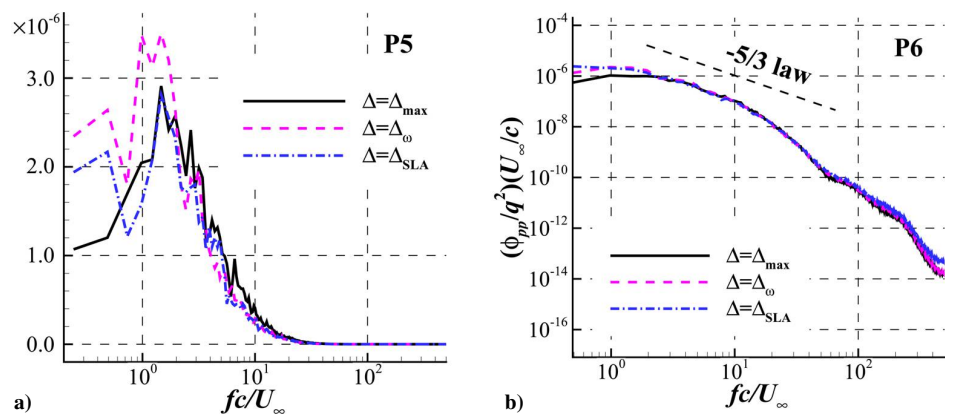


Fig. 14 PSD of pressure fluctuations at points P5 and P6.

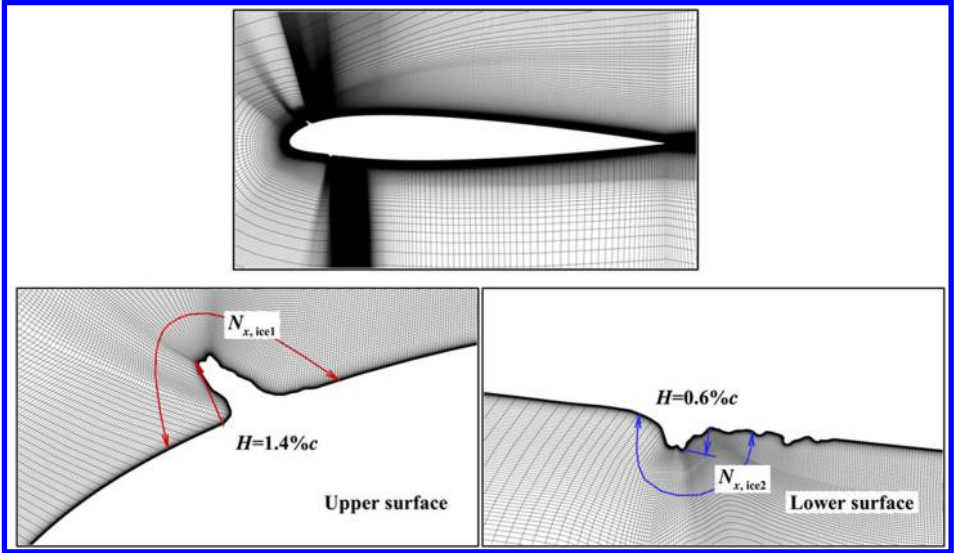


Fig. 15 Computational configuration with baseline grid in x-y plane for NACA-23012/EG1159.

Table 5 Grid information for NACA-23012/EG1159

Cases	N_x	N_z	$N_{x,ice1}$	$N_{x,ice2}$	N_{total} (millions)	L_z/c	$\Delta y_w/c$
Coarse grid	828	80	96	72	9.16	0.1	1.5×10^{-6}
Baseline grid	986	100	114	88	17.47	0.1	1.2×10^{-6}
Fine grid	1190	120	136	108	32.50	0.1	0.9×10^{-6}

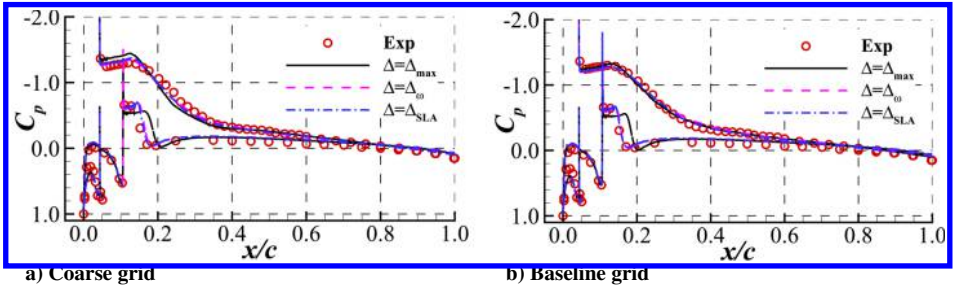


Fig. 16 Mean surface pressure coefficients from experiments [27] and computations.

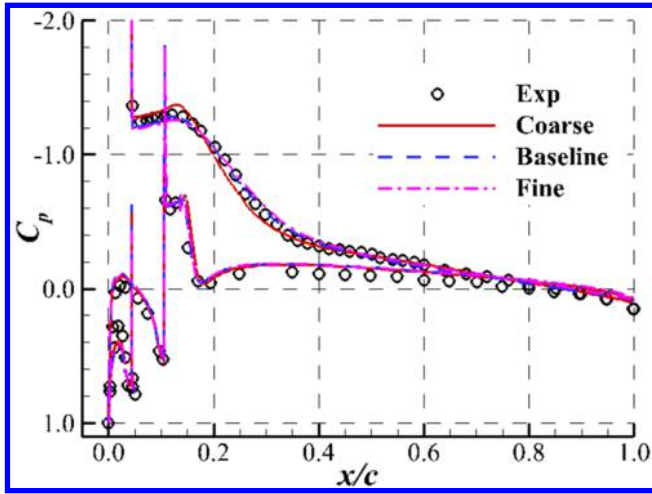


Fig. 17 Mean surface pressure coefficients for three grids with $\Delta = \Delta_{SLA}$.

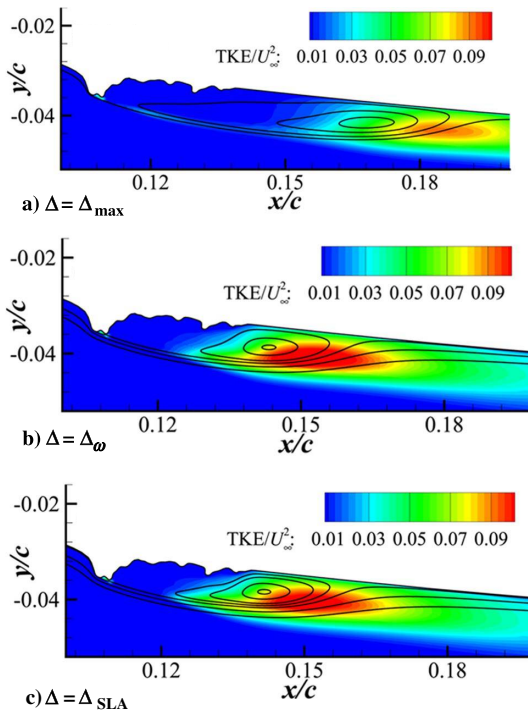


Fig. 18 Mean separation bubbles in contours of mean resolved TKE/U_∞^2 for baseline grid for NACA-23012/EG1159.

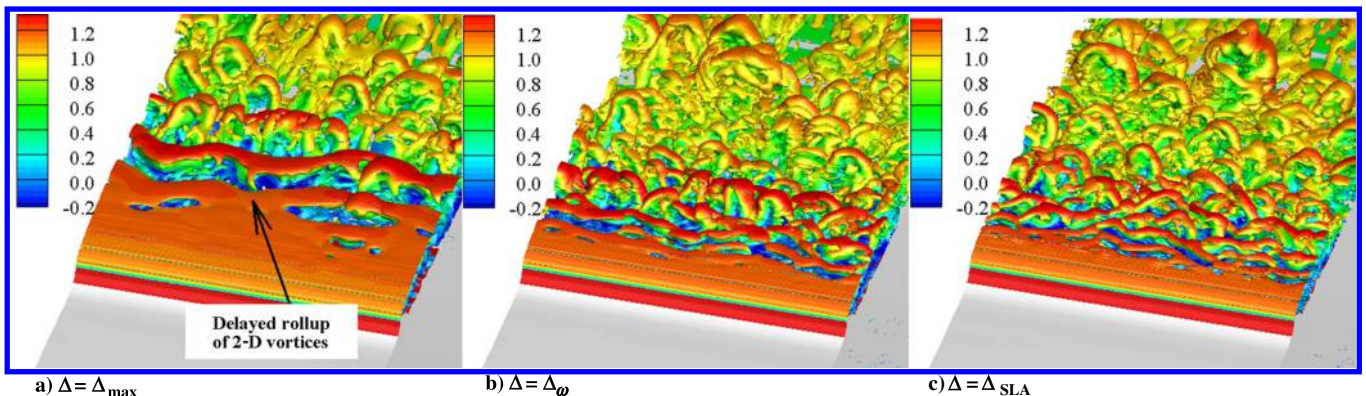


Fig. 19 Isosurfaces of $Q(c/U_\infty)^2 = 500$ downstream of lower surface ice for NACA-23012/EG1159.

using both Δ_ω and Δ_{SLA} but appear much further downstream for $\Delta = \Delta_{max}$.

IV. Conclusions

In this study, two novel subgrid length scales, Δ_ω and Δ_{SLA} , are used to improve the IDDES prediction of flow around an airfoil accreted with horn or ridge ice. The superiority of the two length scales over the original Δ_{max} is demonstrated for two horn-ice cases (GLC-305/944 and NLF-0414/623) and a ridge-ice case (NACA-23012/EG1159).

In contrast to using Δ_{max} , using Δ_ω or Δ_{SLA} produces results in agreement with experiments in terms of the average velocity, pressure, and fluctuation fields for the two horn-ice cases. In more detail, using the novel length scales correctly captures the pattern of vortex rollup and pairing in the initial SSL, and it yields turbulent mixing before reattachment that is consistent with experimental observations. Using the two novel length scales can also correctly predict vortex-shedding frequencies near the reattachment region and introduce reasonable dissipation levels further downstream.

For the ridge-ice case, IDDES combined with Δ_ω or Δ_{SLA} offers clear advantages in capturing ice-induced mild separation bubbles on the lower surface. Using the two novel length scales accelerates the generation of resolved turbulent stresses aft of the ice, which is delayed using Δ_{max} .

Acknowledgments

This work was supported by the National Natural Science Foundation of China (grant nos. 91852108 and 11872230) and the Key Laboratory of Icing and Anti-/De-Icing (grant no. IADL20190201).

References

- [1] Bragg, M. B., Broeren, A. P., and Blumenthal, L. A., "Iced-Airfoil Aerodynamics," *Progress in Aerospace Sciences*, Vol. 41, No. 5, 2005, pp. 323–362.
<https://doi.org/10.1016/j.paerosci.2005.07.001>
- [2] Ansell, P. J., and Bragg, M. B., "Characterization of Low-Frequency Oscillations in the Flowfield About an Iced Airfoil," *AIAA Journal*, Vol. 53, No. 3, 2015, pp. 629–637.
<https://doi.org/10.2514/1.J053206>
- [3] Xiao, M., Zhang, Y., and Zhou, F., "Numerical Investigation of the Unsteady Flow Past an Iced Multi-Element Airfoil," *AIAA Journal*, Vol. 58, No. 9, 2020, pp. 3848–3862.
<https://doi.org/10.2514/1.J059114>
- [4] Gurbachi, H. M., "Ice-Induced Unsteady Flowfield Effects on Airfoil Performance," Ph.D. Thesis, Univ. of Illinois at Urbana-Champaign, Champaign, IL, 2003.
- [5] Stebbins, S. J., Loth, E., Broeren, A. P., and Potapczuk, M., "Review of Computational Methods for Aerodynamic Analysis of Iced Lifting Surfaces," *Progress in Aerospace Sciences*, Vol. 111, Nov. 2019, Paper 100583.
<https://doi.org/10.1016/j.paerosci.2019.100583>
- [6] Marongiu, C., Vitagliano, P. L., Zanazzi, G., and Narducci, R., "Aerodynamic Analysis of an Iced Airfoil at Medium/High Reynolds

- Number," *AIAA Journal*, Vol. 46, No. 10, 2008, pp. 2469–2478.
<https://doi.org/10.2514/1.34550>
- [7] Pan, J., and Loth, E., "Detached Eddy Simulations for Iced Airfoils," *Journal of Aircraft*, Vol. 42, No. 6, 2005, pp. 1452–1461.
<https://doi.org/10.2514/1.11860>
- [8] Alam, M. F., Thompson, D. S., and Walters, D. K., "Hybrid Reynolds-Averaged Navier–Stokes/Large-Eddy Simulation Models for Flow Around an Iced Wing," *Journal of Aircraft*, Vol. 52, No. 1, 2015, pp. 244–256.
<https://doi.org/10.2514/1.C032678>
- [9] Zhang, H., Li, J., and Gong, Z., "Numerical Simulation of the Stalled Separated Flow Around an Iced Airfoil Based on IDDES," *Acta Aerodynamica Sinica*, Vol. 34, No. 3, 2016, pp. 283–288.
<https://doi.org/10.7638/kqdlxxb-2015.0223>
- [10] Xiao, M., Zhang, Y., and Chen, H., "Numerical Study of an Iced Airfoil Using Window-Embedded RANS/LES Hybrid Method," *9th AIAA Atmospheric and Space Environments Conference*, AIAA Paper 2017-3761, 2017.
- [11] Hu, S., Zhang, C., Liu, H., and Wang, F., "Study on Vortex Shedding Mode on the Wake of Horn/Ridge Ice Contamination under High-Reynolds Conditions," *Journal of Aerospace Engineering*, Vol. 233, No. 13, 2019, pp. 5045–5056.
<https://doi.org/10.1177/0954410019835971>
- [12] Gritskevich, M. S., Garbaruk, A. V., Schütze, J., and Menter, F. R., "Development of DDES and IDDES Formulations for the $k-\omega$ Shear Stress Transport Model," *Flow, Turbulence and Combustion*, Vol. 88, No. 3, 2012, pp. 431–449.
<https://doi.org/10.1007/s10494-011-9378-4>
- [13] Mockett, C., Fuchs, M., Garbaruk, A., Shur, M., Spalart, P., Strelets, M., Thiele, F., and Travin, A., "Two Non-Zonal Approaches to Accelerate RANS to LES Transition of Free Shear Layers in DES," *Progress in Hybrid RANS-LES Modelling*, Springer, New York, 2015, pp. 187–201.
https://doi.org/10.1007/978-3-319-15141-0_15
- [14] Chauvet, N., Deck, S., and Jacquin, L., "Zonal Detached Eddy Simulation of a Controlled Propulsive Jet," *AIAA Journal*, Vol. 45, No. 10, 2007, pp. 2458–2473.
<https://doi.org/10.2514/1.28562>
- [15] Shur, M. L., Spalart, P. R., Strelets, M. K., and Travin, A. K., "An Enhanced Version of DES with Rapid Transition from RANS to LES in Separated Flows," *Flow, Turbulence and Combustion*, Vol. 95, No. 4, 2015, pp. 709–737.
<https://doi.org/10.1007/s10494-015-9618-0>
- [16] Xiao, M., Zhang, Y., and Zhou, F., "Numerical Study of Iced Airfoils with Horn Features Using Large-Eddy Simulation," *Journal of Aircraft*, Vol. 56, No. 1, 2019, pp. 94–107.
<https://doi.org/10.2514/1.C034986>
- [17] Chen, H., Li, Z., and Zhang, Y., "U or V Shape: Dissipation Effects on Cylinder Flow Implicit Large-Eddy Simulation," *AIAA Journal*, Vol. 55, No. 2, 2017, pp. 459–473.
<https://doi.org/10.2514/1.J055278>
- [18] Liu, J., Zhu, W., Xiao, Z., Sun, H., Huang, Y., and Liu, Z., "DDES with Adaptive Coefficient for Stalled Flows Past a Wind Turbine Airfoil," *Energy*, Vol. 161, Oct. 2018, pp. 846–858.
<https://doi.org/10.1016/j.energy.2018.07.176>
- [19] Broeren, A. P., Bragg, M. B., and Addy, H. E., "Flowfield Measurements About an Airfoil with Leading-Edge Ice Shapes," *Journal of Aircraft*, Vol. 43, No. 4, 2006, pp. 1226–1234.
<https://doi.org/10.2514/1.19021>
- [20] Mogili, P., Thompson, D., Choo, Y., and Addy, H., "RANS and DES Computations for a Wing with Ice Accretion," *43rd AIAA Aerospace Sciences Meeting and Exhibit*, AIAA Paper 2005-1372, 2005.
- [21] Addy, H., and Chung, J., "A Wind Tunnel Study of Icing Effects on a Natural Laminar Flow Airfoil," *38th Aerospace Sciences Meeting and Exhibit*, AIAA Paper 2000-0095, 2000.
- [22] Choo, Y. K., Thompson, D., and Mogili, P., "Detached-Eddy Simulations of Separated Flow Around Wings with Ice Accretions: Year One Report," National Aeronautics and Space Administration, NASA/CR-2004-213379, 2004.
- [23] Huerre, P., and Monkewitz, P. A., "Local and Global Instabilities in Spatially Developing Flows," *Annual Review of Fluid Mechanics*, Vol. 22, No. 1, 1990, pp. 473–537.
<https://doi.org/10.1146/annurev.fl.22.010190.002353>
- [24] Deck, S., and Laraufie, R., "Numerical Investigation of the Flow Dynamics Past a Three-Element Aerofoil," *Journal of Fluid Mechanics*, Vol. 732, Oct. 2013, pp. 401–444.
<https://doi.org/10.1017/jfm.2013.363>
- [25] Mabey, D. G., "Analysis and Correlation of Data on Pressure Fluctuations in Separated Flow," *Journal of Aircraft*, Vol. 9, No. 9, 1972, pp. 642–645.
<https://doi.org/10.2514/3.59053>
- [26] Ansell, P. J., and Bragg, M. B., "Unsteady Modes in Flowfield About Airfoil with Horn-Ice Shape," *Journal of Aircraft*, Vol. 53, No. 2, 2016, pp. 475–486.
<https://doi.org/10.2514/1.C033421>
- [27] Broeren, A. P., Whalen, E. A., Busch, G. T., and Bragg, M. B., "Aerodynamic Simulation of Runback Ice Accretion," *Journal of Aircraft*, Vol. 47, No. 3, 2010, pp. 924–939.
<https://doi.org/10.2514/1.46475>
- [28] Costes, M., and Moens, F., "Advanced Numerical Prediction of Iced Airfoil Aerodynamics," *Aerospace Science and Technology*, Vol. 91, Aug. 2019, pp. 186–207.
<https://doi.org/10.1016/j.ast.2019.05.010>
- [29] Zhang, Y., Habashi, W. G., and Khurram, R. A., "Zonal Detached-Eddy Simulation of Turbulent Unsteady Flow over Iced Airfoils," *Journal of Aircraft*, Vol. 53, No. 1, 2016, pp. 168–181.
<https://doi.org/10.2514/1.C033253>

C. Wen
Associate Editor